

# Synthesis and physical properties of perovskite $\text{Sm}_{1-x}\text{Sr}_x\text{NiO}_3$ ( $x = 0, 0.2$ ) and infinite-layer $\text{Sm}_{0.8}\text{Sr}_{0.2}\text{NiO}_2$ nickelates

Chengping He, Xue Ming, Qing Li, Xiyu Zhu\*, Jin Si and Hai-Hu Wen\*

Center for Superconducting Physics and Materials, National Laboratory of Solid State Microstructures and Department of Physics, Collaborative Innovation Center of Advanced Microstructures, Nanjing University, Nanjing 210093, China

E-mail: zhuxiyu@nju.edu.cn and hhwen@nju.edu.cn

January 2021

**Abstract.** Recently, superconductivity at about 9-15 K was discovered in  $\text{Nd}_{1-x}\text{Sr}_x\text{NiO}_2$  (Nd-112,  $x \approx 0.125-0.25$ ) infinite-layer thin films, which has stimulated enormous interests in related rare-earth nickelates. Usually, the first step to synthesize this 112 phase is to fabricate the  $R\text{NiO}_3$  ( $R$ -113,  $R$ : rare-earth element) phase, however, it was reported that the 113 phase is very difficult to be synthesized successfully due to the formation of unusual  $\text{Ni}^{3+}$  oxidation state. And the difficulty of preparation is enhanced as the ionic radius of rare-earth element decreases. In this work, we report the synthesis and investigation on multiple physical properties of polycrystalline perovskites  $\text{Sm}_{1-x}\text{Sr}_x\text{NiO}_3$  ( $x = 0, 0.2$ ) in which the ionic radius of  $\text{Sm}^{3+}$  is smaller than that of  $\text{Pr}^{3+}$  and  $\text{Nd}^{3+}$  in related superconducting thin films. The structural and compositional analyses conducted by X-ray diffraction and energy dispersive X-ray spectrum reveal that the samples mainly contain the perovskite phase of  $\text{Sm}_{1-x}\text{Sr}_x\text{NiO}_3$  with small amount of NiO impurities. Magnetization and resistivity measurements indicate that the parent phase  $\text{SmNiO}_3$  undergoes a paramagnetic-antiferromagnetic transition at about 224 K on a global insulating background. In contrast, the Sr-doped sample  $\text{Sm}_{0.8}\text{Sr}_{0.2}\text{NiO}_3$  shows a metallic behavior from 300 K down to about 12 K, while below 12 K the resistivity exhibits a slight logarithmic increase. Meanwhile, from the magnetization curves, we can see that a possible spin-glass state occurs below 12 K in  $\text{Sm}_{0.8}\text{Sr}_{0.2}\text{NiO}_3$ . Using a soft chemical reduction method, we also obtain the infinite-layer phase  $\text{Sm}_{0.8}\text{Sr}_{0.2}\text{NiO}_2$  with square  $\text{NiO}_2$  planes. The compound shows an insulating behavior which can be described by the three-dimensional variable-range-hopping model. And superconductivity is still absent in the polycrystalline  $\text{Sm}_{0.8}\text{Sr}_{0.2}\text{NiO}_2$ .

## 1. Introduction

The discovery of high critical temperature superconductivity (HTS) in cuprates in 1986 [1] created a new era for research of superconductivity. However, after great efforts by many scientists, there are still a lot of puzzlings about the superconducting mechanism

of cuprates [2]. One of the effective ways to resolve these puzzlings is to explore other new superconductors which are isostructural and isoelectronic to the cuprates [3, 4]. Considering the proximity of nickel and copper in the periodic table, it is natural to raise the question that whether the cuprate-like electronic structure or even superconductivity could be realized in nickelates. If so, this would help to understand the nature of HTS in cuprates. Early theoretical studies proposed that layered nickelates with square planar  $\text{NiO}_2$  sheets and the  $\text{Ni}^{1+}$  oxidation state (supposed to give an  $S = 1/2$  magnetic moment) may be analogous to the parent phase of cuprates. By doping holes into the system, superconductivity like that in cuprate superconductors may be realized in nickelates [5, 6]. And this has come true experimentally in  $\text{Nd}_{1-x}\text{Sr}_x\text{NiO}_2$  ( $0.125 < x < 0.25$ ) [7, 8, 9] and  $\text{Pr}_{0.8}\text{Sr}_{0.2}\text{NiO}_2$  [10] thin films deposited on  $\text{SrTiO}_3$  substrates with transition temperatures at about 9-15 K and 7-12 K, respectively. Since the superconductivity in the infinite-layer nickelates was discovered in thin films, it is of great interest to know whether it can be realized in bulk form. However, the recent transport measurements on bulk  $\text{Nd}_{1-x}\text{Sr}_x\text{NiO}_2$  samples show insulating behaviors at both ambient and high pressures [11, 12]. Thus the key question is to know what makes the results in thin films and in bulk samples so contradictory. Since the  $\text{Nd}_{1-x}\text{Sr}_x\text{NiO}_2$  and  $\text{Pr}_{0.8}\text{Sr}_{0.2}\text{NiO}_2$  thin films were grown on  $\text{SrTiO}_3$  substrates, one plausible explanation is that the substrates may play a crucial role in the emergence of superconductivity [13, 14, 15]. As mentioned by Li et al. [7], the films experience compressive strain on the  $\text{SrTiO}_3$  substrates. And the smaller lattice constant may be more conducive to superconductivity [16]. Following this idea, it may be a good way to simulate the strain effect of substrates on the films by replacing  $\text{Nd}^{3+}$  or  $\text{Pr}^{3+}$  with smaller rare-earth cation  $\text{Sm}^{3+}$ .

Looking back to literatures, it is found that the  $R\text{NiO}_3$  perovskites have been intensively studied [17, 18, 19, 20, 21, 22, 23] due to their metal-insulator (MI) transitions and paramagnetic-antiferromagnetic transitions. Except for  $\text{LaNiO}_3$  which has a different crystal structure (rhombohedral) from other  $R\text{NiO}_3$  and is a paramagnetic metal in the whole measured temperature range [24],  $R\text{NiO}_3$  perovskites are paramagnetic metals at high temperatures, while they are in an insulating and antiferromagnetic state at low temperatures [25]. For  $R = \text{Pr}$  and  $\text{Nd}$ , the MI transition temperature ( $T_{\text{MI}}$ ) is the same as the paramagnetic-antiferromagnetic transition temperature ( $T_{\text{N}}$ ) [26]. However, for  $R = \text{Sm}$  or smaller rare-earth ions,  $T_{\text{MI}}$  is usually higher than  $T_{\text{N}}$ . In the region between  $T_{\text{MI}}$  and  $T_{\text{N}}$ ,  $R\text{NiO}_3$  are paramagnetic insulators. The value of  $T_{\text{MI}}$  is strongly dependent on the ionic radius of the rare-earth ions [27]. As the ionic radius decreases, the tolerance factor for stabilizing a regular perovskite structure becomes smaller. The decreased tolerance factor further lead to the reduction of Ni-O-Ni bond angle. Thus the bandwidth which is composed of Ni-3d and O-2p orbitals [28] is also reduced. In this case, the physical properties of  $R\text{NiO}_3$  can be tuned by a variety of methods such as the displacement of rare-earth elements, chemical doping, pressure, temperature, and so on. For  $\text{SmNiO}_3$ , it has been reported that  $T_{\text{MI}}$  and  $T_{\text{N}}$  are 403 K and 225 K, respectively [19]. And crystal symmetry changes

from the high-temperature orthorhombic structure (space group: Pbnm) to the low-temperature monoclinic structure (space group: P2<sub>1</sub>/n) [15, 29, 30]. High pressure studies have shown that the pressure is beneficial to the metallic state and drives the MI transition temperature to a lower value [31, 32]. Furthermore, due to the difficulty in the fabrication of bulk samples, previous researches mainly focused on thin films and heterostructures [15, 25]. To our knowledge, there is no study on the doping effect of bulk SmNiO<sub>3</sub>. Therefore, it is interesting to know whether it will show some novel physical properties upon doping in bulk samples.

Motivated by the reasonings above, in this paper, we report the synthesis and investigation on multiple physical properties of Sm<sub>1-x</sub>Sr<sub>x</sub>NiO<sub>3</sub> ( $x = 0, 0.2$ ) and Sm<sub>0.8</sub>Sr<sub>0.2</sub>NiO<sub>2</sub> polycrystalline samples. The powder X-ray diffraction (XRD) measurements have confirmed the perovskite structures for Sm<sub>1-x</sub>Sr<sub>x</sub>NiO<sub>3</sub> ( $x = 0, 0.2$ ) and infinite-layer structure for Sm<sub>0.8</sub>Sr<sub>0.2</sub>NiO<sub>2</sub>. The compositional analyses show that the Ni occupancy is slightly lower than the nominal value in all three samples and there is a certain strontium distribution in Sm<sub>0.8</sub>Sr<sub>0.2</sub>NiO<sub>3</sub> and Sm<sub>0.8</sub>Sr<sub>0.2</sub>NiO<sub>2</sub>. For SmNiO<sub>3</sub>, the paramagnetic-antiferromagnetic transition appears at about 224 K on an insulating background. Upon Sr doping, Sm<sub>0.8</sub>Sr<sub>0.2</sub>NiO<sub>3</sub> exhibits a metallic behavior accompanied with a resistivity upturn at low temperatures, which seems to be fitted fairly well by the picture concerning magnetic Kondo scattering. The magnetization curves of Sm<sub>0.8</sub>Sr<sub>0.2</sub>NiO<sub>3</sub> show paramagnetic behaviors with a possible spin-glass state below 12 K. After doing soft chemical reduction from Sm<sub>0.8</sub>Sr<sub>0.2</sub>NiO<sub>3</sub>, we successfully synthesize Sm<sub>0.8</sub>Sr<sub>0.2</sub>NiO<sub>2</sub> samples. The Sm<sub>0.8</sub>Sr<sub>0.2</sub>NiO<sub>2</sub> shows an insulating behavior which can be well fitted with three-dimensional (3D) variable-range-hopping (VRH) model ( $\ln\rho \propto T^{-1/4}$ ) in the whole measured temperature range. There is no sign of superconductivity above 2 K in the polycrystalline Sm<sub>0.8</sub>Sr<sub>0.2</sub>NiO<sub>2</sub>.

## 2. Experimental methods

Polycrystalline samples of Sm<sub>1-x</sub>Sr<sub>x</sub>NiO<sub>3</sub> ( $x = 0, 0.2$ ) were successfully synthesized under high pressure and high temperature by solid-state reaction method. First, the precursors Sm<sub>2-2x</sub>Sr<sub>2x</sub>NiO<sub>4</sub> ( $x = 0, 0.2$ ) were prepared by calcining stoichiometric amounts of Sm<sub>2</sub>O<sub>3</sub> (99.9%, Alfa Aesar), NiO (99.0%, Alfa Aesar) and SrO (99.9%, Strem Chemicals) at 1200 °C for 24 h. Then the precursors Sm<sub>2-2x</sub>Sr<sub>2x</sub>NiO<sub>4</sub>, NiO and KClO<sub>4</sub> (99.0%, Alfa Aesar) were weighed in a molar ratio of 1:1:2, mixed and ground thoroughly in an agate mortar. Subsequently, the mixture was pressed into pellets and sealed in a gold capsule. These procedures were carried out in a glove box filled with purified Ar gas (H<sub>2</sub>O, O<sub>2</sub> <0.1 ppm). The gold capsule with the mixed compounds was then placed in a BN capsule and heated up to 1000 °C and kept at this temperature for 2 h under the pressure of 2 GPa in a piston-cylinder high pressure apparatus (LPC 250-300/50, Max Voggenreiter). Then the samples were rapidly cooled to room temperature in 1 min followed by the release of pressure. The obtained samples were washed with distilled water to dissolve KCl and unreacted KClO<sub>4</sub>, and then dried.

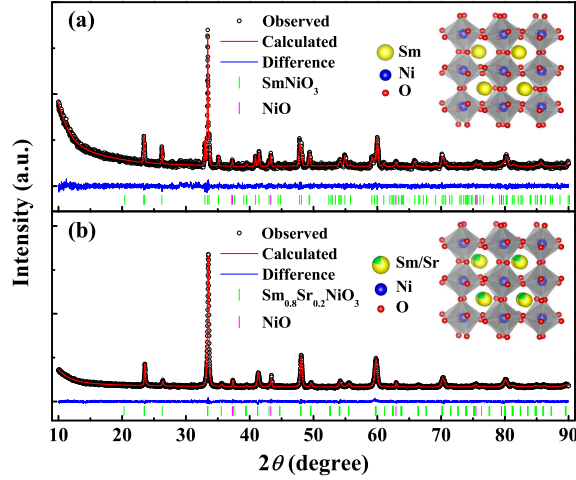


**Figure 1.** Powder X-ray diffraction patterns (black circles) and Rietveld refinement fitting curves (red lines) of (a)  $\text{SmNiO}_3$  and (b)  $\text{Sm}_{0.8}\text{Sr}_{0.2}\text{NiO}_3$ . The insets of (a) and (b) show the schematic crystal structures of  $\text{SmNiO}_3$  and  $\text{Sm}_{0.8}\text{Sr}_{0.2}\text{NiO}_3$ , respectively.

The sample  $\text{Sm}_{0.8}\text{Sr}_{0.2}\text{NiO}_2$  was obtained by reacting  $\text{Sm}_{0.8}\text{Sr}_{0.2}\text{NiO}_3$  with  $\text{CaH}_2$  (98.5%, Aladdin) through a soft chemical reduction method. Appropriate amounts of  $\text{Sm}_{0.8}\text{Sr}_{0.2}\text{NiO}_3$  and 0.1 g of  $\text{CaH}_2$  powder were pressed into pellets respectively and then sealed in an evacuated quartz tube. Note that the  $\text{Sm}_{0.8}\text{Sr}_{0.2}\text{NiO}_3$  and  $\text{CaH}_2$  pellets were placed at different positions in the quartz tube to avoid direct contact. The quartz tube was heated to 340 °C at a rate of 10 °C/min and sustained at this temperature for 10 h. We have also tried to reduce  $\text{SmNiO}_3$  with  $\text{CaH}_2$  in order to obtain  $\text{SmNiO}_2$ , but failed probably because of the instability of  $\text{Ni}^{1+}$  oxidation state [12].

The phase identification of the prepared samples was carried out by powder XRD (Bruker D8 Advance) with  $\text{Cu-K}\alpha$  radiation and the TOPAS 4.2 software [33] was used to refine the crystal structures by Rietveld analysis [34]. Micrographs of the samples were taken by a scanning electron microscopy (SEM) (Phenom ProX, Phenom World) and the chemical composition analyses were done with an energy dispersive X-ray spectrum (EDS) which is an option of the SEM. The dc magnetization was collected on a vibrating sample magnetometer (PPMS-VSM 9T, Quantum Design). The electrical resistivities of the samples were measured by the standard four-probe method using the physical property measurement system (PPMS 16T, Quantum Design).

### 3. Results and discussion

#### 3.1. $\text{Sm}_{1-x}\text{Sr}_x\text{NiO}_3$ ( $x = 0, 0.2$ )

*3.1.1. Sample characterization* Figure 1 shows the powder XRD patterns of (a)  $\text{SmNiO}_3$  and (b)  $\text{Sm}_{0.8}\text{Sr}_{0.2}\text{NiO}_3$  polycrystalline samples with Rietveld refinements. Except for several minor peaks of NiO impurities, all other peaks belong to the perovskite  $\text{SmNiO}_3$  and  $\text{Sm}_{0.8}\text{Sr}_{0.2}\text{NiO}_3$  phases which can be well indexed with an orthorhombic unit cell (space group: Pbnm). Their schematic crystal structures have been illustrated

**Table 1.** Crystallographic data of SmNiO<sub>3</sub> and Sm<sub>0.8</sub>Sr<sub>0.2</sub>NiO<sub>3</sub> at room temperature.

fomula	SmNiO <sub>3</sub>	Sm <sub>0.8</sub> Sr <sub>0.2</sub> NiO <sub>3</sub>
space group	<i>Pbnm</i>	<i>Pbnm</i>
<i>a</i> (Å)	5.3241(6)	5.3641(8)
<i>b</i> (Å)	5.4282(2)	5.3564(8)
<i>c</i> (Å)	7.5594(7)	7.5675(8)
<i>V</i> (Å <sup>3</sup> )	218.4743(9)	217.4405(1)
$\rho$ (g/cm <sup>3</sup> )	7.815	7.469
$R_{wp}$ (%)	4.80	3.24
$R_p$ (%)	3.77	2.55
<i>GOF</i>	1.10	1.11

in the insets of Fig. 1(a) and Fig. 1(b), where the yellow/green, blue and red spheres represent the Sm/Sr, Ni and O atoms, respectively. The perovskite structure is distorted because of the relative small ionic radius of Sm<sup>3+</sup> cation, and the NiO<sub>6</sub> octahedra are tilted for optimizing the Sm-O distances. The corner-sharing octahedra are arranged along three directions of the crystal and Sm<sup>3+</sup> cations occupy the space between these NiO<sub>6</sub> octahedra. The cell parameters obtained from Rietveld refinement profiles are  $a = 5.3241(6)$  Å,  $b = 5.4282(2)$  Å,  $c = 7.5594(7)$  Å for SmNiO<sub>3</sub> and  $a = 5.3641(8)$  Å,  $b = 5.3564(8)$  Å,  $c = 7.5675(8)$  Å for Sm<sub>0.8</sub>Sr<sub>0.2</sub>NiO<sub>3</sub>, which are consistent with previous studies [21, 35, 36]. It can be seen that the lattice constant  $c$  expands slightly after Sr doping, which is reasonable since the ionic radius of Sr<sup>2+</sup> (118 pm) is larger than that of Sm<sup>3+</sup> (95.8 pm) [37]. The crystallographic parameters and the reliability factors have been listed in Table 1. The small values of  $R_{wp}$  and  $R_p$  indicate that the fittings are considerably good.

Figure 2 presents the SEM images of (a) SmNiO<sub>3</sub> and (b) Sm<sub>0.8</sub>Sr<sub>0.2</sub>NiO<sub>3</sub> samples. It can be seen clearly that both samples contain two types of grains, which are the major part of the grains with argenteous color and a small amount of dark gray ones. Then we perform EDS analyses to get a deeper understanding of the element composition. We measure 18 spots for both samples randomly, which have been marked by the red crosses in the two images. Note that we prepared the samples in stoichiometry. However, by analyzing the Sr content and Ni occupancy normalized by the concentration of Sm for SmNiO<sub>3</sub> and (Sm+Sr) for Sm<sub>0.8</sub>Sr<sub>0.2</sub>NiO<sub>3</sub>, we find that both of them deviate slightly from the nominal values. Namely, the argenteous grains correspond to the composition of SmNi<sub>1- $\delta$</sub> O<sub>3</sub> for SmNiO<sub>3</sub> and Sm<sub>1- $y$</sub> Sr <sub>$y$</sub> Ni<sub>1- $\delta$</sub> O<sub>3</sub> for Sm<sub>0.8</sub>Sr<sub>0.2</sub>NiO<sub>3</sub>, respectively. And the small amount of dark gray grains are NiO, which is consistent with the XRD results. Fig. 2(c) presents the Ni occupancy of different spots for SmNiO<sub>3</sub> and Sm<sub>0.8</sub>Sr<sub>0.2</sub>NiO<sub>3</sub>.

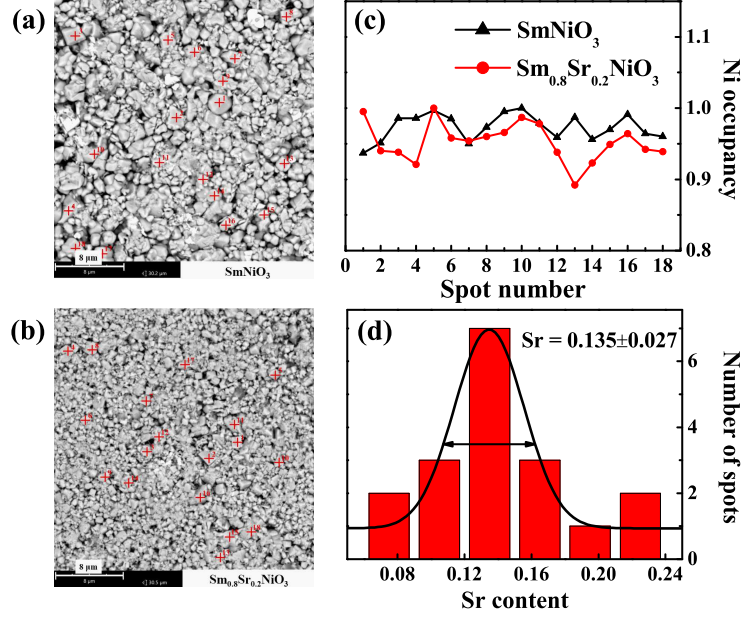


**Figure 2.** SEM images of (a) SmNiO<sub>3</sub> and (b) Sm<sub>0.8</sub>Sr<sub>0.2</sub>NiO<sub>3</sub>. (c) Ni occupancy in SmNiO<sub>3</sub> and Sm<sub>0.8</sub>Sr<sub>0.2</sub>NiO<sub>3</sub>. (d) Compositional distribution of Sr content with Gaussian fitting for Sm<sub>0.8</sub>Sr<sub>0.2</sub>NiO<sub>3</sub>.

The Ni occupancy changes slightly and the mean values are about 0.97(4) for SmNiO<sub>3</sub> and 0.95(3) for Sm<sub>0.8</sub>Sr<sub>0.2</sub>NiO<sub>3</sub>. Both values are slightly lower than the nominal one. Note that R. Jaramillo et al. [38] did EDS measurements on SmNiO<sub>3</sub> thin films and found the ratio of Sm to Ni is around 1.1 with an error of 0.1 but without the indication of Ni deficiency. Since the accuracy of EDS measurement depends on the calibration of the system, sample morphology and the actual location of the energy spectrum from the calculated elements, there are experimental errors in EDS analysis. Thus, whether there is Ni deficiency in the samples requires further experiments. Fig. 2(d) shows the compositional distribution of Sr content with Gaussian fitting for Sm<sub>0.8</sub>Sr<sub>0.2</sub>NiO<sub>3</sub>. The Sr content is randomly distributed in Sm<sub>0.8</sub>Sr<sub>0.2</sub>NiO<sub>3</sub> and the average value obtained from the fitting is  $0.135 \pm 0.027$ , which is close to the nominal value and implies the successful doping of Sr. In addition, the full width at half maximum (FWHM) of the XRD peak at around 26° for Sm<sub>0.8</sub>Sr<sub>0.2</sub>NiO<sub>3</sub> is 0.24, which is larger than the value of 0.15 for SmNiO<sub>3</sub>. The broader peak indicates smaller grains in Sm<sub>0.8</sub>Sr<sub>0.2</sub>NiO<sub>3</sub> or the Sr concentration has a distribution in the grains. Since the spot number in Fig. 2(c) is sorted by the increase of Sr content, there is no apparent correlation between Sr content and Ni occupancy among different spots.

*3.1.2. Magnetic and electrical transport properties* Figure 3(a) displays the temperature dependences of magnetic moment at the field of 1 T in zero-field-cooling (ZFC) and field-cooling (FC) modes for SmNiO<sub>3</sub>. As we can see, the magnetic moment increases smoothly with decreasing temperature from 300 K to about 224 K and a small kink is observed at 224 K (see the enlarged ZFC curve in the inset of Fig. 3(a)),

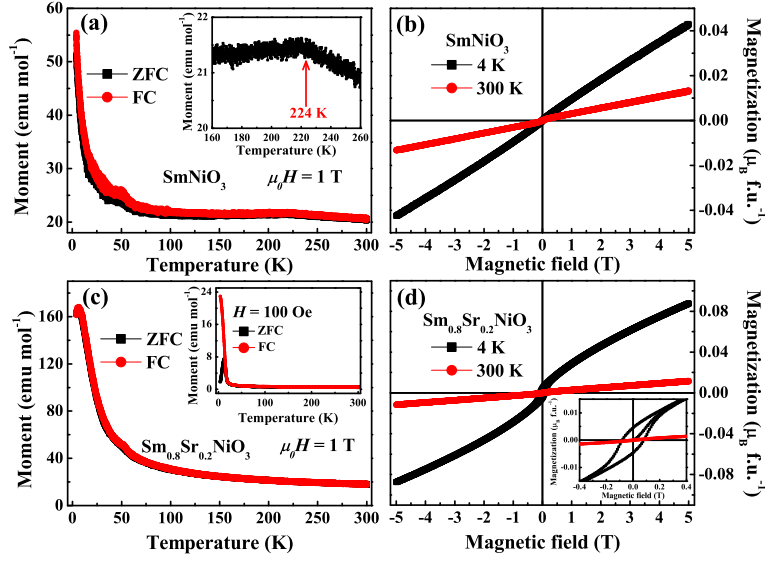


**Figure 3.** Temperature dependences of magnetic moment measured in both ZFC and FC modes at 1 T for (a)  $\text{SmNiO}_3$  and (c)  $\text{Sm}_{0.8}\text{Sr}_{0.2}\text{NiO}_3$ . The insets of (a) and (c) show the enlarged view around the paramagnetic-antiferromagnetic transition for  $\text{SmNiO}_3$  and temperature dependences of magnetic moment in ZFC and FC modes at 100 Oe for  $\text{Sm}_{0.8}\text{Sr}_{0.2}\text{NiO}_3$ , respectively. Magnetization hysteresis loops measured at 4 K and 300 K for (b)  $\text{SmNiO}_3$  and (d)  $\text{Sm}_{0.8}\text{Sr}_{0.2}\text{NiO}_3$ . The inset of (d) shows the zoom-in view of the loops at low fields for  $\text{Sm}_{0.8}\text{Sr}_{0.2}\text{NiO}_3$ .

which is consistent with previous reports and has been attributed to the paramagnetic-antiferromagnetic transition [19, 29]. An abnormal hump-like behavior is observed at about 50 K, which is attributed to the antiferromagnetic transition of frozen oxygen. We have also measured the magnetization hysteresis at 4 K and 300 K for  $\text{SmNiO}_3$  and present the results in Fig. 3(b). Both curves are roughly linear and the magnetization is unsaturated up to the field of 5 T, which rule out the possibility of ferromagnetic component. After Sr doping, the magnetic moment of  $\text{Sm}_{0.8}\text{Sr}_{0.2}\text{NiO}_3$  increases with temperature cooling down, while a drop appears below 7 K, which are shown in Fig. 3(c). To illustrate the small drop at low temperatures, we measure the temperature dependences of magnetic moment in ZFC and FC modes under the field of 100 Oe, and present the results in the inset of Fig. 3(c). A clear magnetic irreversibility occurs below 12 K between ZFC and FC curves. Besides, in Fig. 3(d), we perform the magnetization hysteresis loops measured at 4 K and 300 K for  $\text{Sm}_{0.8}\text{Sr}_{0.2}\text{NiO}_3$ . The linear  $M(H)$  relation at 300 K demonstrates a paramagnetic like behavior. However, an obvious deviation from linearity is observed from the curve of  $\text{Sm}_{0.8}\text{Sr}_{0.2}\text{NiO}_3$  at 4 K. The small magnetic hysteresis demonstrates a weak ferromagnetic behavior. The weak ferromagnetic behavior at low temperatures seen in  $M-H$  curves has been also observed in  $\text{BiNiO}_3$  [28] and  $\text{PbNiO}_3$  [39], and has been attributed to the canted spins or the magnetic impurity phases. Combined with  $M-T$  and  $M-H$  results in  $\text{Sm}_{0.8}\text{Sr}_{0.2}\text{NiO}_3$ , the low-temperature magnetization behaviors observed here are more likely related to a spin-glass state. Similar behaviors have been found in Ca-doped  $\text{Lu}_{1-x}\text{Ca}_x\text{MnO}_3$  single

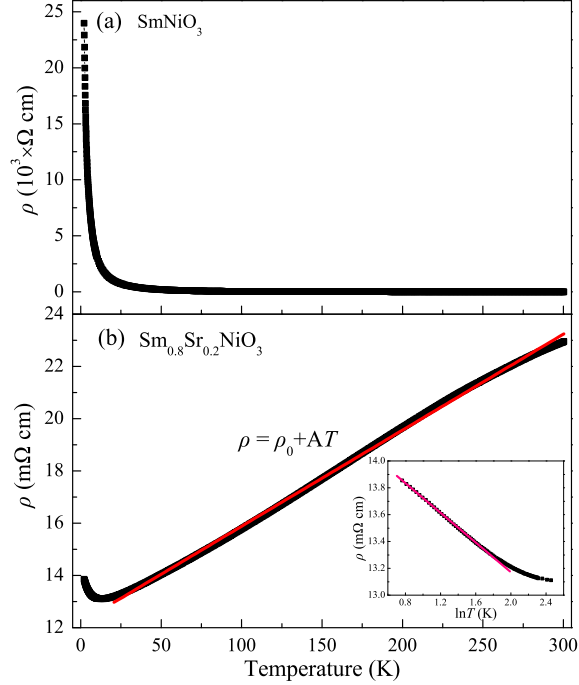


**Figure 4.** Temperature dependences of resistivity for (a)  $\text{SmNiO}_3$  and (b)  $\text{Sm}_{0.8}\text{Sr}_{0.2}\text{NiO}_3$ . The inset of (b) shows the logarithmic temperature dependence of resistivity at low temperature for  $\text{Sm}_{0.8}\text{Sr}_{0.2}\text{NiO}_3$ .

crystals [40], Mn-doped  $\text{CaNiGeH}$  [41] and  $\text{KCr}_3\text{As}_3$  [42]. But we can not exclude the possibility that the behaviors in our samples are caused by impurities or the canted spins. Further study is needed in order to clarify the origin of the low-temperature magnetization behaviors in  $\text{Sm}_{0.8}\text{Sr}_{0.2}\text{NiO}_3$ .

Figure 4 shows the comparison of the temperature dependences of resistivity for (a)  $\text{SmNiO}_3$  and (b)  $\text{Sm}_{0.8}\text{Sr}_{0.2}\text{NiO}_3$ .  $\text{SmNiO}_3$  exhibits an insulating behavior in the whole measured temperature range from 2 K to 300 K, which is consistent with previous reports [25, 19]. In order to better understand the transport behavior of  $\text{SmNiO}_3$ , we have tried to fit the data with several models, such as the band-gap model ( $\ln\rho \propto 1/T$ ), small-polaron-hopping (SPH) model ( $\ln(\rho/T) \propto -1/T$ ) and 3D VRH model ( $\ln\rho \propto T^{-1/4}$ ) [43], but all failed. We should note that the oxygen nonstoichiometry usually occurs in  $R\text{NiO}_3$  nickelates due to the instability of  $\text{Ni}^{3+}$  oxidation state [44]. And the oxygen deficiency in the sample plays an important role in transport properties, just like the cases in cuprates and other nickelates [45, 46, 47, 48]. Furthermore, since the pellets used for resistivity measurements were pressed by powder, the grain boundary is another nonnegligible factor which can affect the transport properties [49]. These factors may lead to the exotic scattering in  $\text{SmNiO}_3$  polycrystals which can not be understood by present models and is different from that in thin films, in which the insulating behavior can be fitted by the VRH model [50]. In contrast,  $\text{Sm}_{0.8}\text{Sr}_{0.2}\text{NiO}_3$  shows a metallic behavior above 12 K with a resistivity upturn at lower temperatures. As we can see in Fig. 4(b), the  $\rho - T$  curve is roughly linear between 12 K and 300 K,

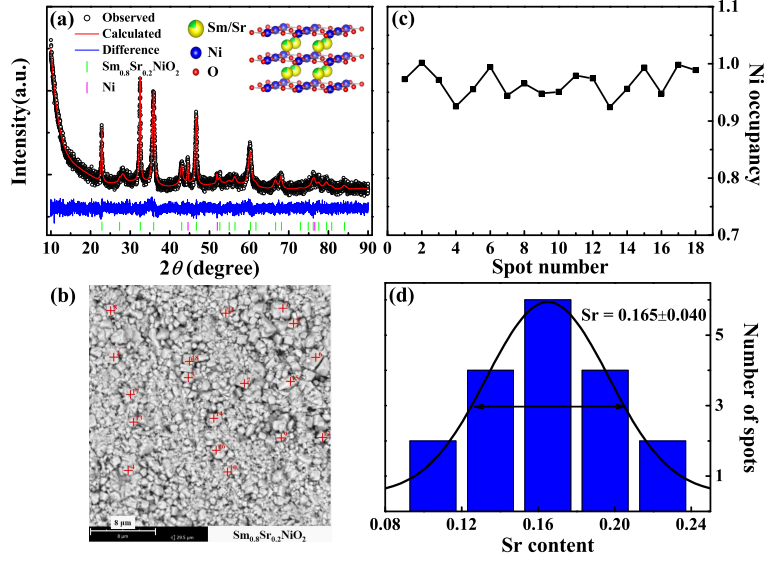


**Figure 5.** Powder X-ray diffraction pattern (black circles) and Rietveld refinement fitting curve (red line) for  $\text{Sm}_{0.8}\text{Sr}_{0.2}\text{NiO}_2$ . The inset shows the crystal structure of  $\text{Sm}_{0.8}\text{Sr}_{0.2}\text{NiO}_2$ . (b) SEM image of  $\text{Sm}_{0.8}\text{Sr}_{0.2}\text{NiO}_2$ . (c) Ni occupancy and (d) compositional distribution of Sr concentration with Gaussian fitting for  $\text{Sm}_{0.8}\text{Sr}_{0.2}\text{NiO}_2$ .

so we attempt to fit the data using the formula  $\rho(T) = \rho_0 + AT$  and the fitting result has been depicted by the red line. The fitting result yields  $\rho_0 = 12.21 \text{ m}\Omega \text{ cm}$  and  $A = 3.68 \times 10^{-2} \text{ m}\Omega \text{ cm K}^{-1}$ . The metallic behavior observed here may be caused by hole doping through Sr substitution, and has also been observed in bulk  $\text{Nd}_{0.8}\text{Sr}_{0.2}\text{NiO}_3$  [12]. The low-temperature resistivity upturn can be fitted well by the logarithmic function, namely  $\rho \propto \ln T$  (see the inset in Fig. 4(b)), which can be attributed to the magnetic Kondo scattering. In this scenario, partial localized Ni-3d electrons carry magnetic moments which serve as the Kondo-scattering centers and thus result in the scattering of conducting electrons [51, 52, 53]. In addition, the grain boundary may also result in the low-temperature resistivity upturn, since the pellets used for resistivity measurements were pressed by powder.

### 3.2. $\text{Sm}_{0.8}\text{Sr}_{0.2}\text{NiO}_2$

**3.2.1. Sample characterization** Using a soft chemical reduction method, we successfully obtain the  $\text{Sm}_{0.8}\text{Sr}_{0.2}\text{NiO}_2$  polycrystalline samples from the prepared perovskite  $\text{Sm}_{0.8}\text{Sr}_{0.2}\text{NiO}_3$ . Figure 5(a) displays the powder XRD pattern of  $\text{Sm}_{0.8}\text{Sr}_{0.2}\text{NiO}_2$  sample with Rietveld refinement. And the inset presents the schematic crystal structure. Except for 2-3 minor peaks of Ni impurities, all other peaks correspond to the infinite-layer  $\text{Sm}_{0.8}\text{Sr}_{0.2}\text{NiO}_2$  phase which can be well indexed with a tetragonal unit cell (space group:  $P4/mmm$ ). Analogous to the case in our reported  $\text{Nd}_{0.8}\text{Sr}_{0.2}\text{NiO}_2$  samples [11], the low crystallinity (inferred from the relatively low intensity of the XRD peaks) is observed in  $\text{Sm}_{0.8}\text{Sr}_{0.2}\text{NiO}_2$ , which is a common feature of soft chemical reduction method [54]. And

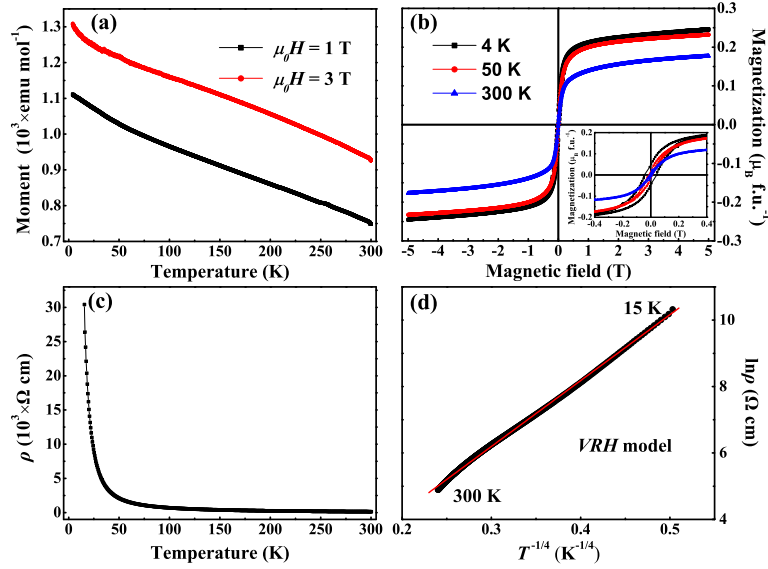


**Figure 6.** (a) Temperature dependences of magnetic moment measured in ZFC mode at 1 T and 3 T for  $\text{Sm}_{0.8}\text{Sr}_{0.2}\text{NiO}_2$ . (b) Magnetization hysteresis loops measured at 4 K, 50 K and 300 K. The inset of (b) shows the zoom-in view of the loops at low fields. (c) Temperature dependence of resistivity for  $\text{Sm}_{0.8}\text{Sr}_{0.2}\text{NiO}_2$ . (d) The curve of  $\ln \rho$  versus  $T^{-1/4}$  (VRH model).

there are also a few broad peaks which can be attributed to the low crystallinity and the buckling of  $\text{NiO}_2$  planes. The cell parameters obtained from Rietveld refinement profile are  $a = b = 3.8885(3) \text{ \AA}$  and  $c = 3.2572(0) \text{ \AA}$ . The reliability factors and the goodness of fit are  $R_{wp} = 3.46\%$ ,  $R_p = 2.75\%$  and  $\text{GOF} = 1.09$ . The lattice constants are smaller than those of bulk  $\text{Nd}_{0.8}\text{Sr}_{0.2}\text{NiO}_2$ , which is reasonable due to the smaller ionic radius of  $\text{Sm}^{3+}$  than that of  $\text{Nd}^{3+}$ . Fig. 5(b) shows the SEM image of  $\text{Sm}_{0.8}\text{Sr}_{0.2}\text{NiO}_2$ , which contains the main  $\text{Sm}_{1-y}\text{Sr}_y\text{Ni}_{1-\delta}\text{O}_2$  grains and a small amount of Ni impurities from the EDS analyses. Using the same way as that for  $\text{Sm}_{1-x}\text{Sr}_x\text{NiO}_3$  ( $x = 0, 0.2$ ) to analyze the EDS data, we display the Ni occupancy of 18 spots in Fig. 5(c). The mean value of Ni occupancy is  $0.96(6)$ , which is close to that in bulk  $\text{Nd}_{0.8}\text{Sr}_{0.2}\text{NiO}_2$  [11]. Fig. 5(d) shows the compositional distribution of Sr content with Gaussian fitting for  $\text{Sm}_{0.8}\text{Sr}_{0.2}\text{NiO}_2$ . The Sr content is randomly distributed in  $\text{Sm}_{0.8}\text{Sr}_{0.2}\text{NiO}_2$  and the average value obtained from the fitting is  $0.165 \pm 0.040$ . Once again, there is no direct relationship between the Ni occupancy and Sr content.

**3.2.2. Magnetic and electrical transport properties** Figure 6(a) shows the temperature dependences of magnetic moment measured in ZFC mode under the fields of 1 T and 3 T. The magnetic moment increases almost linearly with the decrease of temperature at 1 T and 3 T. And the two curves are roughly parallel to each other. This is different from the behavior of bulk  $\text{Nd}_{0.8}\text{Sr}_{0.2}\text{NiO}_2$  [11], in which a paramagnetic Curie-Weiss tail was observed at low temperatures. The magnetization hysteresis loops, shown in Fig. 6(b), provide further information about the magnetic behavior. The  $M$ - $H$

curves show clear S-shaped hysteresis loops, indicating a weak ferromagnetic component in the paramagnetic background. As in bulk  $\text{Nd}_{0.8}\text{Sr}_{0.2}\text{NiO}_2$  [11], the ferromagnetic and paramagnetic component can be attributed to the segregated Ni impurities and the main  $\text{Sm}_{0.8}\text{Sr}_{0.2}\text{NiO}_2$  phase, respectively. The different behaviors of magnetic properties between  $\text{Sm}_{0.8}\text{Sr}_{0.2}\text{NiO}_2$  and  $\text{Nd}_{0.8}\text{Sr}_{0.2}\text{NiO}_2$  may be attributed to the different proportion of Ni impurities in the two samples or the intrinsic properties originated from  $\text{Sm}_{0.8}\text{Sr}_{0.2}\text{NiO}_2$ . In current situation, the ferromagnetic moment contributed by the Ni impurity seems to be close to that of the bulk  $\text{Nd}_{0.8}\text{Sr}_{0.2}\text{NiO}_2$ , while the low temperature Curie-Weiss term seems to be much smaller, suggesting a smaller paramagnetic contribution in  $\text{Sm}_{0.8}\text{Sr}_{0.2}\text{NiO}_2$ . Further study is needed to clarify the origin of the magnetic behaviors in  $\text{Sm}_{0.8}\text{Sr}_{0.2}\text{NiO}_2$ .

Figure 6(c) shows the temperature dependence of electrical resistivity for  $\text{Sm}_{0.8}\text{Sr}_{0.2}\text{NiO}_2$ . Clearly the sample  $\text{Sm}_{0.8}\text{Sr}_{0.2}\text{NiO}_2$  exhibits an insulating behavior. We have also tried to fit the data using different models in order to reveal the nature of its insulating behavior and find that the  $\rho(T)$  curve can only be well fitted in the whole measured temperature range by the 3D VRH model (shown in Fig. 6(d)), which has also been observed in bulk  $\text{Nd}_{0.8}\text{Sr}_{0.2}\text{NiO}_2$  [11],  $\text{NdNiO}_3$  thin films [55] and  $\text{Nd}_{1.67}\text{Sr}_{0.33}\text{NiO}_4$  polycrystals [56]. The VRH conduction indicates a strong localization behavior and usually occurs in disordered or correlated systems [57]. The VRH conduction observed here suggests the existence of disorder and/or strong correlation effect in  $\text{Sm}_{0.8}\text{Sr}_{0.2}\text{NiO}_2$ . The insulating behavior may get reasons from grain boundary scattering and disorders in the synthesized samples. There is still no sign of superconductivity in  $\text{Sm}_{0.8}\text{Sr}_{0.2}\text{NiO}_2$ .

#### 4. Conclusions

In summary, we have successfully synthesized the perovskite  $\text{Sm}_{1-x}\text{Sr}_x\text{NiO}_3$  ( $x = 0, 0.2$ ) and infinite-layer  $\text{Sm}_{0.8}\text{Sr}_{0.2}\text{NiO}_2$  polycrystalline samples. From XRD and EDS analyses, the Ni occupancy in all the three samples deviates slightly from the nominal value and the Sr content is unevenly distributed in  $\text{Sm}_{0.8}\text{Sr}_{0.2}\text{NiO}_3$  and  $\text{Sm}_{0.8}\text{Sr}_{0.2}\text{NiO}_2$ . The sample  $\text{SmNiO}_3$  undergoes an antiferromagnetic transition at about 224 K on an insulating background. However after Sr doping,  $\text{Sm}_{0.8}\text{Sr}_{0.2}\text{NiO}_3$  becomes a metal and a possible spin-glass state is observed below 12 K from the magnetization measurements. The  $\text{Sm}_{0.8}\text{Sr}_{0.2}\text{NiO}_2$  sample exhibits an insulating behavior and superconductivity is still absent in the present compound. These results provide some useful information of the Sm derivative nickelates, and also clues for the realization of superconductivity in bulk nickelates.

#### Acknowledgments

This work was supported by the National Key R&D Program of China (Grant No. 2016YFA0300401 and 2016YFA0401704), National Natural Science Foundation of China (Grant No. A0402/11534005 and E0209/52072170), and the Strategic Priority Research

Program of Chinese Academy of Sciences (Grant No. XDB25000000).

## References

- [1] Bednorz J G and Müller K A 1986 *Z. Phys. B* **64** 189-93
- [2] Keimer B, Kivelson S A, Norman M R, Uchida S and Zaanen J 2015 *Nature* **518** 179-86
- [3] Zhang J, Botana A S, Freeland J W, Phelan D, Zheng H, Pardo V, Norman M R and Mitchell J F 2017 *Nature Phys.* **13** 864-9
- [4] Chaloupka J and Khaliullin G 2008 *Phys. Rev. Lett.* **100** 016404
- [5] Anisimov V I, Bukhvalov D and Rice T M 1999 *Phys. Rev. B* **59** 7901-6
- [6] Botana A S, Pardo V and Norman M R 2017 *Phys. Rev. Materials* **1** 021801
- [7] Li D, Lee K, Wang B Y, Osada M, Crossley S, Lee H R, Cui Y, Hikita Y and Hwang H Y 2019 *Nature* **572** 624-7
- [8] Li D, Wang B Y, Lee K, Harvey S P, Osada M, Goodge B H, Kourkoutis L F and Hwang H Y 2020 *Phys. Rev. Lett.* **125** 027001
- [9] Zeng S, Tang C S, Yin X, Li C, Li M, Huang Z, Hu J, Liu W, Omar G J, Jani H, Lim Z S, Han K, Wan D, Yang P, Pennycook S J, Wee A T S and Ariando A 2020 *Phys. Rev. Lett.* **125** 147003
- [10] Osada M, Wang B Y, Goodge B H, Lee K, Yoon H, Sakuma K, Li D, Miura M, Kourkoutis L F and Hwang H Y 2020 *Nano Lett.* **20** 5735-40
- [11] Li Q, He C, Si J, Zhu X, Zhang Y and Wen H H 2020 *Commun. Mater.* **1** 16
- [12] Wang B X, Zheng H, Krivyakina E, Chmaissem O, Lopes P P, Lynn J W, Gallington L C, Ren Y, Rosenkranz S, Mitchell J F and Phelan D 2020 *Phys. Rev. Materials* **4** 084409
- [13] Zhou X R, Feng Z X, Qin P X, Yan H, Hu S, Guo H X, Wang X N, Wu H J, Zhang X, Chen H Y, Qiu X P and Liu Z Q 2020 *Rare Met.* **39** 368-74
- [14] Kumar A, Singh P, Kaur D, Jesudasan J and Raychaudhuri P 2006 *J. Phys. D: Appl. Phys.* **39** 5310-5
- [15] Catalan G 2008 *Phase Transit.* **81** 729-49
- [16] Sakakibara H, Usui H, Suzuki K, Kotani T, Aoki H and Kuroki K 2020 *Phys. Rev. Lett.* **125** 077003
- [17] Wold A, Post B and Banks E 1957 *J. Am. Chem. Soc.* **79** 4911-3
- [18] Granados X, Fontcuberta J, Obradors X, Mañosa LI and Torrance J B 1993 *Phys. Rev. B* **48** 11666-72
- [19] Mroginiski M A, Massa N E, Salva H, Alonso J A and Martínez-Lope M J 1999 *Phys. Rev. B* **60** 5304-11
- [20] Alonso J A, Martínez-Lope M J, Casais M T, Martínez J L, Demazeau G, Largeteau A, García-Muñoz J L, Muñoz A and Fernández-Díaz M T 1999 *Chem. Mater.* **11** 2463-9
- [21] Alonso J A, Martínez-Lope M J, Casais M T, Aranda M A G and Fernández-Díaz M T 1999 *J. Am. Chem. Soc.* **121** 4754-62
- [22] Alonso J A, García-Muñoz J L, Fernández-Díaz M T, Aranda M A G, Martínez-Lope M J and Casais M T 1999 *Phys. Rev. Lett.* **82** 3871-4
- [23] Medarde M, Dallera C, Grioni M, Delley B, Vernay F, Mesot J, Sikora M, Alonso J A and Martínez-Lope M J 2009 *Phys. Rev. B* **80** 245105
- [24] Sreedhar K, Honig J M, Darwin M, McElfresh M, Shand P M, Xu J, Crooker B C and Spalek J 1993 *Phys. Rev. B* **46** 6382-6
- [25] Catalano S, Gibert M, Fowlie J, Íñiguez J, Triscone J M and Kreisel J 2018 *Rep. Prog. Phys.* **81** 046501
- [26] García-Muñoz J L, Rodríguez-Carvajal J, Lacorre P and Torrance J B 1992 *Phys. Rev. B* **46** 4414-25
- [27] Torrance J B, Lacorre P, Nazzari A I, Ansaldo E J and Niedermayer Ch 1992 *Phys. Rev. B* **45** 8209-12

- [28] Ishiwata S, Azuma M, Takano M, Nishibori E, Takata M, Sakata M and Kato K 2002 *J. Mater. Chem.* **12** 3733-7
- [29] Rodríguez-Carvajal J, Rosenkranz S, Medarde M, Lacorre P, Fernandez-Díaz M T, Fauth F and Trounov V 1998 *Phys. Rev. B* **57** 456-64
- [30] Serrano-Sánchez F, Fauth F, Martínez J L and Alonso J A 2019 *Inorg. Chem.* **58** 11828-35
- [31] Amboage M, Hanfland M, Alonso J A and Martínez-Lope M J 2005 *J. Phys.: Condens. Matter* **17** S783-8
- [32] Zhou J S, Goodenough J B and Dabrowski B 2005 *Phys. Rev. Lett.* **95** 127204
- [33] Cheary R W and Coelho A 1992 *J. Appl. Cryst.* **25** 109-21
- [34] Rietveld H M 1969 *J. Appl. Cryst.* **2** 65-71
- [35] Pérez-Cacho J, Blasco J, García J and Sanchez R 2000 *J. Solid State Chem.* **150** 145-53
- [36] Henry P F, Weller M T and Wilson C C 2002 *Chem. Mater.* **14** 4104-10
- [37] Biswas P, Kumar V, Agarwal G, Ntwaeaborwa O M and Swart H C 2016 *Ceram. Int.* **42** 2317-23
- [38] Jaramillo R, Schoofs F, Ha S D and Ramanathan S 2013 *J. Mater. Chem. C* **1** 2455-62
- [39] Inaguma Y, Tanaka K, Tsuchiya T, Mori D, Katsumata T, Ohba T, Hiraki K i, Takahashi T and Saitoh H 2011 *J. Am. Chem. Soc.* **133** 16920-9
- [40] Cheng P, Sun W, Fang Y, Kang B, Lv W, Xiao Q, Zhang J and Chen F 2020 *Ceram. Int.* **46** 15958-62
- [41] Liu X, Matsuishi S, Fujitsu S, Ishigaki T, Kamiyama T and Hosono H 2012 *J. Am. Chem. Soc.* **134** 11687-94
- [42] Bao J K, Li L, Tang Z T, Liu Y, Li Y K, Bai H, Feng C M, Xu Z A and Cao G H 2015 *Phys. Rev. B* **91** 180404
- [43] Lin H, Si J, Zhu X, Cai K, Li H, Kong L, Yu X and Wen H H 2018 *Phys. Rev. B* **98** 075132
- [44] Nikulin I V, Novojilov M A, Kaul A R, Mudretsova S N and Kondrashov S V 2004 *Mater. Res. Bull.* **39** 775-91
- [45] Fratini M, Poccia N, Ricci A, Campi G, Burghammer M, Aeppli G and Bianconi A 2010 *Nature* **466** 841-4
- [46] Li J, Pellicciari J, Mazzoli C, Catalano S, Simmons F, Sadowski J T, Levitan A, Gibert M, Carlson E, Triscone J M, Wilkins S and Comin R 2019 *Nat. Commun.* **10** 4568
- [47] Campi G, Bianconi A, Poccia N, Bianconi G, Barba L, Arrighetti G, Innocenti D, Karpinski J, Zhigadlo N D, Kazakov S M, Burghammer M, Zimmermann M v, Sprung M and Ricci A 2015 *Nature* **525** 359-62
- [48] Sayagués M J, Vallet-Regí M, Caneiro A and González-Calbet J M 1994 *J. Solid State Chem.* **110** 295-304
- [49] Li Q, Si J, Duan T, Zhu X and Wen H H 2020 *Philos. Mag.* **100** 2402-15
- [50] Shukla N, Joshi T, Dasgupta S, Borisov P, Lederman D and Datta S 2014 *Appl. Phys. Lett.* **105** 012108
- [51] Li B Z, Wang C, Yang P T, Sun J P, Liu Y B, Wu J, Ren Z, Cheng J G, Zhang G M and Cao G H 2020 *Phys. Rev. B* **101** 195142
- [52] Zhang G M, Yang Y F and Zhang F C 2020 *Phys. Rev. B* **101** 020501
- [53] Li Q, He C, Zhu X, Si J, Fan X and Wen H H 2021 *Sci. China-Phys. Mech. Astron.* **64** 227411
- [54] Zhou X, Wilfong B, Vivanco H, Paglione J, Brown C M and Rodriguez E E 2016 *J. Am. Chem. Soc.* **138** 16432-42
- [55] Catalan G, Bowman R M and Gregg J M 2000 *Phys. Rev. B* **62** 7892-900
- [56] Zaghrioui M, Giovannelli F, Pruvost S, Poirot N and Monot-Laffez I 2006 *J. Magn. Magn. Mater.* **305** 71-5
- [57] Lin Y Q, Chen X M and Liu X Q 2009 *Solid State Commu.* **149** 784-7